RSC Advances

PAPER

View Article Online
View Journal | View Issue

Cite this: *RSC Adv.*, 2026, **16**, 18093

Self-supporting cotton-derived 3D carbon–Si nanoarchitecture for solvent-free fabrication of high-performance lithium-ion anodes

Nguyen Van Tu, *[a] Pham Van Trinh, [a] Nguyen Van Chuc, [a] Cao Thi Thanh,[a] Bui Hung Thang,[a] Pham Thi Nam,[a] Nguyen Hoang Tung,[a] Pham Duy Long,[a] Nguyen Thanh Tung, [a] Tran Dai Lam, [a] Phan Ngoc Minh,[b] Nguyen Van Hao,[c] Vu Xuan Hoa, [c] Vu Van Ngoc,[d] Dinh Trong Thang [d] and Tran Van Hau *[a]

In this work, we report a sustainable, binder-free, and current-collector-free anode architecture based on a cotton-derived three-dimensional nanoarchitectured carbon framework decorated with silicon nanoparticles (3D-CC@Si). The as-prepared 3D carbon scaffold serves simultaneously as the active material, conductive network, and mechanically robust support, enabling direct coin-cell assembly without polymer binders, current collectors, or toxic solvent processing. Structural and morphological characterization results reveal that spherical Si nanoparticles are uniformly anchored and tightly embedded within the porous carbon network, while a conformal amorphous carbon coating is formed on the Si surface, providing effective electrical contact and interfacial stabilization. Benefiting from the synergistic effects of the conductive 3D carbon framework and the carbon-coated Si nanoparticles, the 3D-CC@Si anode exhibits enhanced electrochemical accessibility, improved structural integrity, and excellent electrochemical performance. This work demonstrates a simple, scalable, and environmentally benign strategy for constructing high-performance Si-based anodes, offering a promising pathway toward practical lithium-ion batteries with high energy density.

Received 27th December 2025
Accepted 23rd March 2026

DOI: 10.1039/d5ra10046a

rsc.li/rsc-advances

1. Introduction

Lithium-ion batteries (LIBs) have become the dominant energy storage technology, supporting a wide range of applications from portable electronic devices to electric vehicles (EVs) and large-scale grid energy storage. Their success is due to their high energy density, long cycle life, and good efficiency in comparison to other rechargeable batteries. However, the rapid expansion of markets such as EVs and the widespread integration of renewable energy has placed unprecedented demands on battery power, especially in terms of energy density, safety, and sustainability. Consequently, the rational design and improvement of electrode materials remains a key strategy for enhancing overall battery performance. Among the two electrodes in LIBs, the anode plays a crucial role in determining both capacity and cycling stability. Commercial graphite, which is widely used as an anode material, has a theoretical capacity of only 372 mAh g^{-1}.[1,2] Although graphite offers good electrical conductivity and cycling stability, its limited capacity restricts the achievable energy density of LIBs, thereby hindering their application in next-generation high-energy systems. To overcome this issue, extensive research has focused on the development of alternative anode materials with higher specific capacity.

Silicon (Si) has emerged as one of the most promising candidates due to its high theoretical specific capacity of 4200 mAh g^{-1}, which is about ten times higher than that of conventional graphite. Furthermore, Si has a relatively low lithiation potential (<0.5 V), most abundant element on the Earth's crust.[3,4] These advantages make Si highly attractive for integration into advanced LIB anodes. Despite these merits, however, the commercialization of Si anodes remains severely restricted by intrinsic material limitations. Notably, Si undergoes extreme volume expansion of more than 300% during lithiation, which causes mechanical stress, pulverization, and loss of electrical contact.[5,6] Moreover, its low electrical conductivity and the formation of an unstable solid–electrolyte interphase (SEI) layer during cycling, result in rapid capacity fading and low coulombic efficiency.[7,8] Consequently, strategies that can effectively mitigate these issues are urgently needed to unlock the practical potential of Si-based anodes.

[a]*Institute of Materials Science, Vietnam Academy of Science and Technology, Hanoi, Vietnam. E-mail: tunv@ims.vast.vn; hautv@ims.vast.ac.vn*

[b]*Gruaduate University of Science and Technology, Vietnam Academy of Science and Technology, Hanoi, Vietnam*

[c]*Institute of Science and Technology, TNU-University of Sciences, Thai Nguyen, Vietnam*

[d]*University of Science, Vietnam National University, Hanoi, Vietnam*

One widely accepted approach to address the challenges of Si is to design composite materials by integrating Si nanoparticles (SiNPs) into conductive and robust matrices. Such frameworks can mitigate volume changes of Si, maintain structural integrity, and enhance electrical conductivity, thus improving electrochemical performance. In this context, various types of carbon, such as graphene, carbon nanotubes (CNTs), graphite and amorphous carbon, have been employed to construct Si–C composite matrix.[3,9–12] Although these materials have shown remarkable improvements in performance, their relatively high cost and complex fabrication processes prevent their widespread use in practice.

To overcome these limitations, biomass-derived carbons have recently received growing attention as sustainable, low-cost, and scalable alternatives for energy storage materials.[13–15] Natural biomass is abundant, renewable, and often contains hierarchical porous structures and enriched surface functional groups, which are highly advantageous for electrochemical applications. For example, He *et al.*, embed silicon in natural grape stem biomass-derived porous carbon framework and used it as high performance anode of LIBs. The composite showed an excellent lithium storage performance with a reversible capacity of 891 mAh g^{-1} after 400 cycles at 0.2 A g^{-1}, corresponding to a capacity retention of 88.6%.[15] Meng *et al.*, developed a low-cost anode based on silicon/biomass carbon composite for LIBs. The composite anode could deliver a high reversible specific capacity of 318.4 mAh g^{-1} after 100 cycles at 200 mA g^{-1}.[16]

Recently, cotton, a cellulose-rich biomass, easily carbonized into porous carbon frameworks have received much attention. The inherent fibrous structure of cotton can be tailored to form interconnected conductive networks with large surface areas, which facilitates electrolyte penetration and ion transport. Moreover, cotton-derived carbon can provide sufficient void space to accommodate the volume changes of SiNPs during lithiation/delithiation cycle, thereby reducing mechanical degradation and improving cycling stability. Despite these advantages, relatively few studies have systematically investigated the integration of SiNPs with cotton-derived carbon frameworks.

In this work, the development of a sustainable, binder-free, and current-collector-free anode architecture is highly desirable for realizing the intrinsic advantages of Si while overcoming the limitations of conventional slurry-based electrode fabrication. Herein, we introduce a cotton-derived 3D nanoarchitectured carbon framework decorated with Si nanoparticles (3D-CC@Si) that serves simultaneously as the active material and the mechanically robust, conductive framework. This integrated, self-supporting architecture enables the direct assembly of lithium-ion coin cells without the use of polymeric binders, metal current collectors, or environmentally unfriendly solvent-based processing. Such a simplified and solvent-free manufacturing route not only reduces the complexity and cost of electrode preparation but also enhances structural stability and electrochemical accessibility of the Si active sites. The proposed 3D-CC@Si composite anode thus provides a promising and scalable pathway toward practical, high-performance Si-based lithium-ion batteries.

2. Experiment

2.1 Materials

Bach Tuyet absorbent cotton (100% natural cotton fiber, used for personal hygiene and medical care) was purchased from Bach Tuyet company (Vietnam). Silicon power (99%, 200 mesh) was supplied by Macklin company. Sodium deoxycholate (SDC) surfactant was sourced from Fujifilm company (Japan).

2.2 The preparation of SiNPs

Silicon nanoparticles (SiNPs) were nanonized and sphericalized by using the DC thermal plasma system model M-DC10. A thermal plasma jet was produced *via* ionizing the nitrogen (N_2) passing through the cathode and anode torches. The voltage and current between the cathode and anode were 220 V and 80 A, respectively. The Si source was injected into the center of the plasma zone through the feeder. The torch gas flow rate was set at 80 lpm (liters per minute) *via* a using a mass flow controller, while the carrier gas from the powder feeder to the reactor was fixed at 4 lpm. The total feeding rate of the precursor was set at 5 g min^{-1}. A ring blower was utilized to sustain a pressure of 625 torr in the system during the experiment, ensuring that only the nanonized particles traversed the system and reached the filter.

2.3 The preparation of 3D-CC@Si composite

0.1 g sodium deoxycholate (SDC) surfactant was weighted and dissolved in 50 ml alcohol. Then, different amount of silicon nanoparticles was dispersed into the solution by ultrasonication for 30 min. And then, the cotton was immersed into the solution. Then, the sample was dried gradually. Finally, the sample was loaded into the center of the furnace for 30 min at 800 °C under a mixture of argon and hydrogen to form the composite (Fig. 1).

2.4 The characterization of materials

The surface morphologies of the samples were examized using field emission scanning electron microscopy (FE-SEM, Hitachi S-4800, Japan) at an accelerating voltage of 5 kV, and transmission electron microscopy (TEM, JEM 2100, Joel, Japan) at an accelerating voltage of 200 kV. The crystal structures of the samples were analyzed using Raman spectroscopy at an excitation wavelength of 532 nm. The energy dispersive X-ray spectrum (EDS) mapping of the materials was performed using a scanning electron microscope (SEM) (JSM-IT800, Joel, Japan).

2.5 Electrochemical measurements

The electrochemical measurements were performed through an assembled CR2032-type coin cell (half-cell). The composite was cut into circular electrodes with a diameter of 15 mm. The coin cells were then assembled in a high-purity argon glove box (MTI company, H_2O, O_2 < 1 ppm) using Celgard 2300 as the separator, lithium foil as the counter electrode and 1 M $LiPF_6$ in the solution of 1 : 1 vol ratio of ethylene carbonate (EC) and diethyl carbonate (DEC) as the electrolyte. After assembling, the cyclic voltammetry (CV) curve was performed at scanning rates of

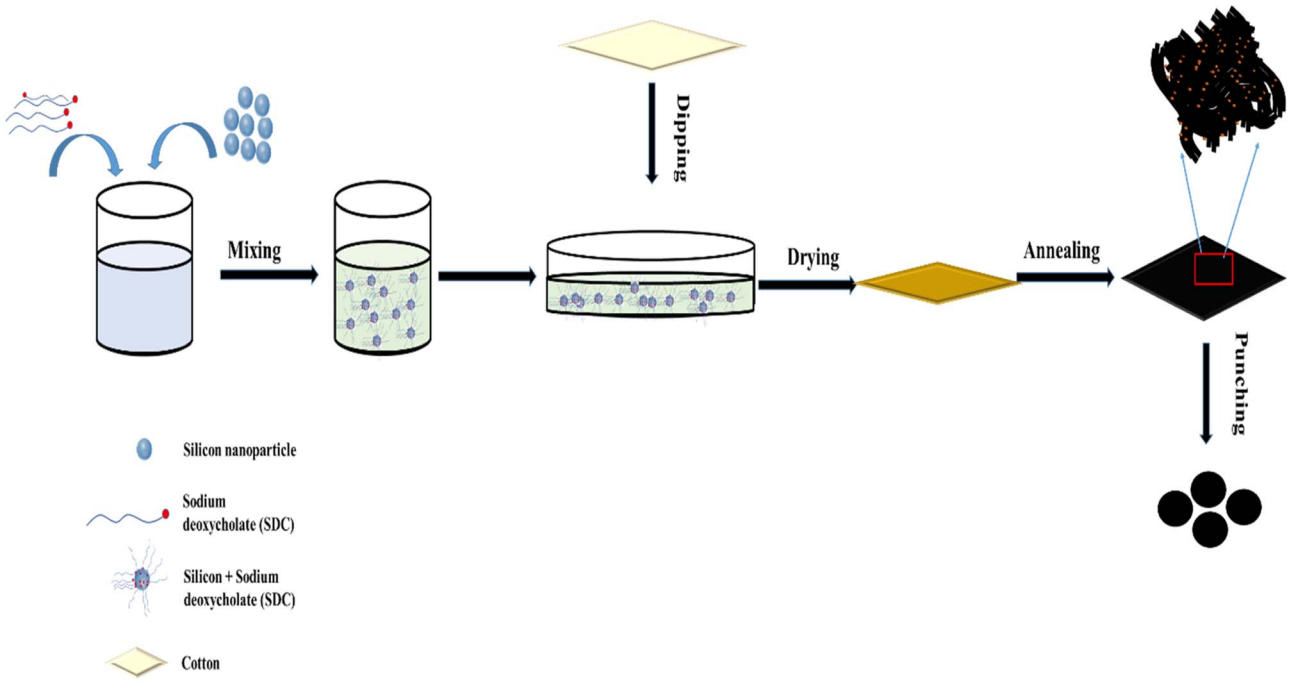

Fig. 1 A schematic diagram for preparation of the 3D-CC@Si composite.

0.01 mV s^{-1} over a potential window of 0.01–3 V using SP-300/240 electrochemical workstation (Bio-Logic SAS, France). Charge–discharge measurements were performed on a multi-channel battery testing system (Neware BTS-5V10 mA, Neware Technology Co., Ltd, China) under different C-rate with the applied voltage ranging from 0.01 to 3 V. The C-rate was calculated based on the theoretical capacity of Si and the theoretical capacity of mesoporous carbon as shown in SI (Table S1).

3. Results and discussion

Fig. 2a displays the SEM picture of raw micro-sized silicon powder, illustrating irregularly shaped particles with a wide size variation from several micrometers to about 100 μm. After DC plasma synthesis, the resulting silicon nanoparticles exhibit a spherical morphology with a diameter in a range of few ten nanometer (nm) to ~800 nm, as illustrated in Fig. 2b.

Fig. 3a is a digital photo of as-received cotton materials. To provide more information on the surface morphology of raw cotton material, SEM was employed. SEM image (Fig. 3c) shows that pristine cotton material is composed of cotton fibers with a typical twisted ribbon-like structure, smooth surfaces (Inset in Fig. 3c), and a relatively uniform width along their length. The fibers are loosely entangled, forming an interconnected network with abundant voids between them. After carbonization process, the white of cotton was turned to black (Fig. 3b). In SEM observations, carbonized fibers appear slightly smaller and more brittle, indicating partial shrinkage due to removal of volatile constituents. The formation of a continuous and

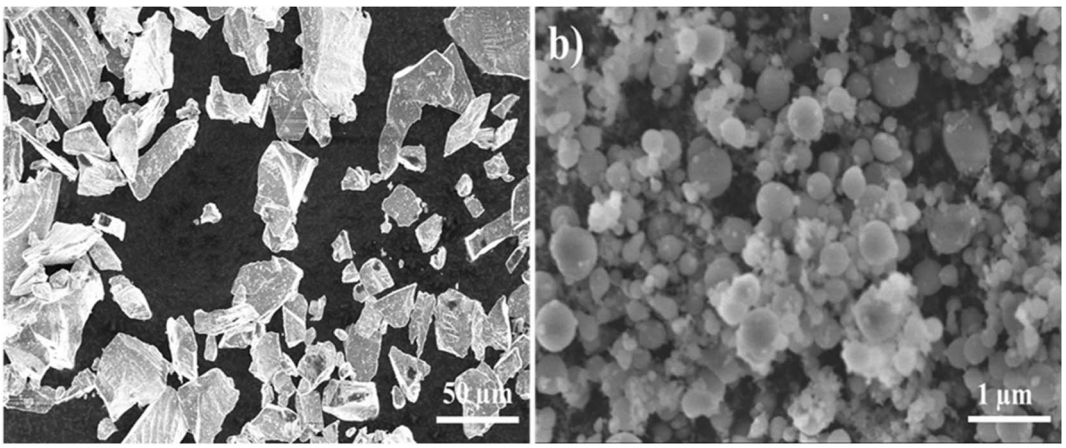

Fig. 2 SEM image of (a) raw micro-sized silicon, (b) As-fabricated silicon nanoparticles (SiNPs).

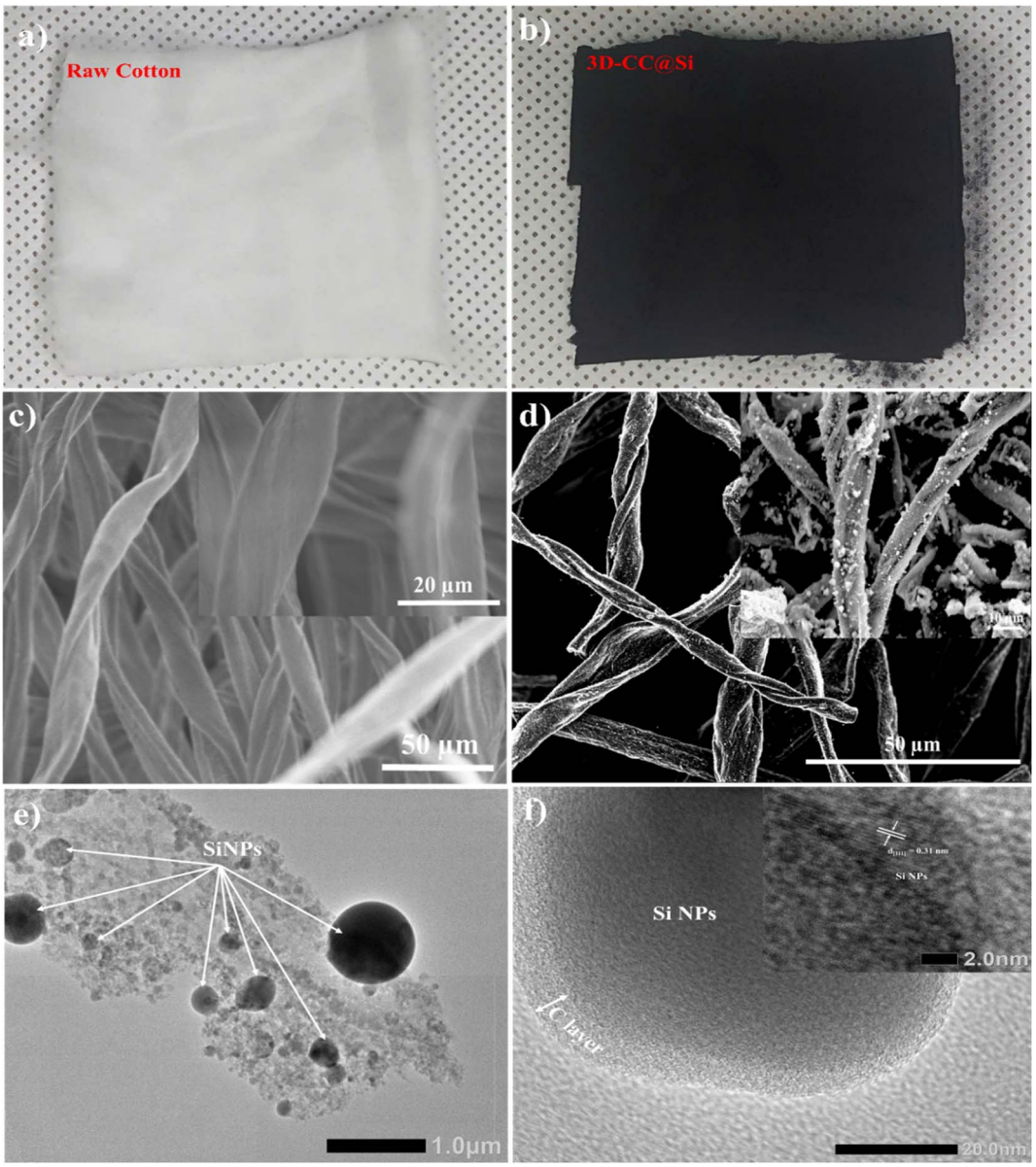

Fig. 3 Digital photo and SEM image of as-received cotton (a and c) and 3D-CC@Si (b and d), Inset in (c) and (d) are the zoomed-in image of pristine cotton fiber and 3D-CC@Si, (e and f) TEM image of 3D-CC@Si.

conductive carbon framework is apparent, while the interconnected structure remains intact (Fig. 3d). This 3D carbon network is expected to facilitate rapid electron transfer and provide mechanical strength, which makes it an ideal framework for integrating active materials into lithium ion battery composite anodes. Besides, numerous Si nanoparticles are homogeneously anchored on the carbonized cotton framework, as clearly shown in the inset of Fig. 3d. The TEM images in Fig. 3e confirm that silicon nanoparticles (SiNPs) are successfully deposited onto the cotton-derived carbon framework. The anchoring of Si nanoparticles onto the three-dimensional carbon framework is mainly attributed to physical confinement and interfacial interactions because carbonized cotton possesses a porous and defect-rich surface with abundant edge sites, which enables the effective immobilization of Si nanoparticles within the interconnected fibrous network. In addition, the carbonization of SDC surfactant on both the carbonized cotton and SiNPs lead to the formation of an outer carbon coating. The HRTEM image (Fig. 3f) further shows the presence of an amorphous carbon coating layer, enveloping the SiNPs. This outer carbon shell is expected to act as an interfacial stabilizer, effectively reducing the direct contact between silicon and the electrolyte, thereby mitigating excessive solid–electrolyte interphase (SEI) formation. Inset in Fig. 3f reveals lattice fringes with *a* spacing of 0.31 nm, which corresponds to the (111) plane of Si. Moreover, the carbon coating enhances electrical conductivity and provides a flexible mechanical buffer, which helps accommodate volume changes of Si and maintain the structural integrity of the electrode during long-term cycling. This close interfacial contact between SiNPs and the

three-dimensional carbon network enhances the overall electrical conductivity and promotes efficient electron and ion transport during the charge–discharge cycles. This result was confirmed by a change in resistance of the samples, as shown in Fig. S1 (SI).

Fig. 4 presents the elemental distribution mapping (EDS) of the 3D nanoarchitectured cotton-derived carbon scaffold decorated with SiNPs. The mapping images clearly demonstrate the uniform distribution of Si throughout the carbon framework, confirming the effective anchoring of SiNPs on the carbonized cotton fibers. The carbon signal (C) is continuously distributed along the fibrous network, while the Si signal appears as finely dispersed spots, indicating that the surfactant-assisted synthesis successfully prevent Si aggregation. In Fig. 4, the apparent discrepancy between the SEM image (Fig. 4a) and the corresponding EDS Si mapping (Fig. 4c) may arise from the different contrast mechanisms and sampling depths of these techniques. The contrast in SEM image is mainly governed by surface topography and local conductivity. Therefore, darker regions may correspond to recessed or porous areas rather than the absence of material. In addition, when the microscope is focused on a specific region to obtain a sharp image, the regions located at lower heights or deeper positions may appear darker due to defocusing effects and reduced electron signal intensity. In contrast, EDS detects X-rays from a relatively large electron–matter interaction volume beneath the surface, allowing Si signals to be detected even in areas that appear dark in the SEM image. The oxygen (O) element observed in the mapping likely originates from residual surface oxides on SiNPs or partially oxidized carbon species. These results provide strong evidence of the homogeneous elemental composition and well-integrated Si-carbon structure, which are expected to contribute to improved electrical contact and structural stability during electrochemical cycling.

To further characterize the materials, the samples were assessed by employing Raman spectroscopy. In Fig. 5a (black curve), the sharp peak at ~520 cm^{-1} is assigned to the Si–Si stretching mode originating from optical phonons in crystalline silicon.[17,18] In the Raman spectrum of pristine cotton fiber (Fig. 5b, red curve), distinct vibrational bands appear at characteristic positions. 330, 377, 433, 454, 897, and 1095, 1120, 1150, 1337, 1379, 1476, 2896. The peaks at 454 and 433 are arised from C–C–O ring deformation modes while those at 373 and 330 are assigned C–O–C glycosidic link deformation and C–C–C ring deformation vibrations, respectively. The 1150 cm^{-1} band is ascribed to C–C ring asymmetric stretching vibrations

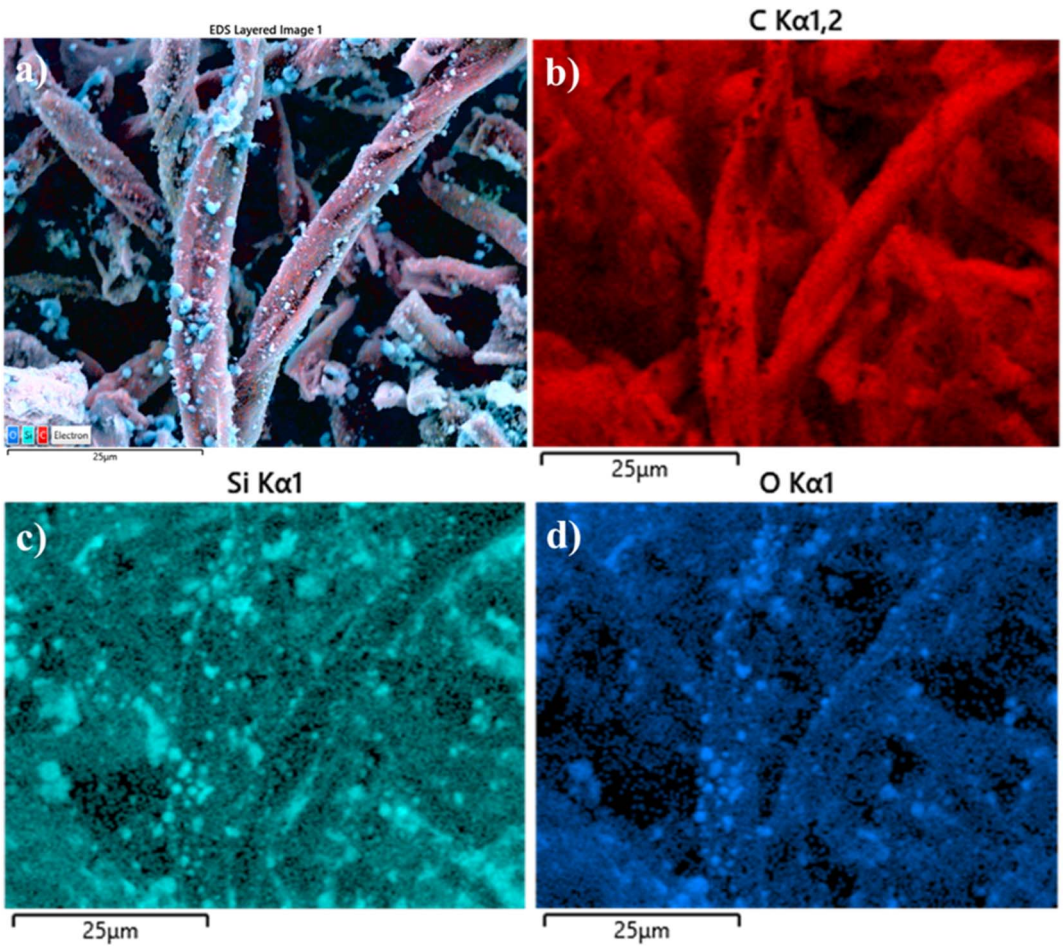

Fig. 4 (a) SEM- EDS mapping of 3D- CC@Si composite. (b–d) EDS mapping for C, Si, and O elements.

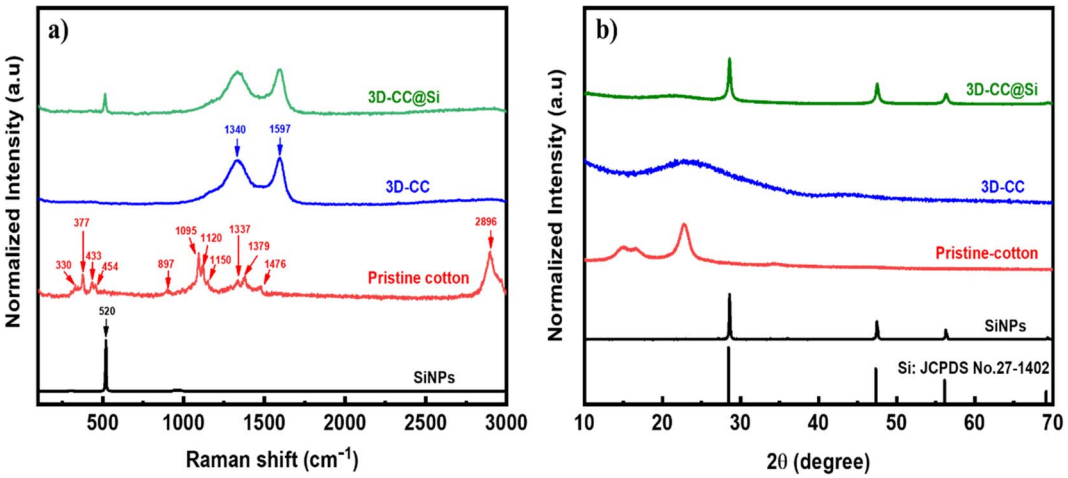

Fig. 5 (a) Raman spectra and (b) XRD patterns of SiNPs, pristine-cotton, 3D-CC, 3D-CC@Si composite.

while the 1095 and 1120 cm^{-1} corresponds to the C–O–C stretching modes of the β-(1 → 4)-glycosidic linkages in the cellulose backbone respectively. Notably, the strong peak at 1095 cm^{-1} is a fingerprint of cellulose crystallinity. Additional bands at around 1337, 1376 cm^{-1} and 1470 cm^{-1} arise from CH and CH_2 deformation vibrations, while broader signals in the 2897 cm^{-1}, originate from C–H stretching in the cellulose chain.[19] The absence of D and G bands, which are typically observed in carbon-based materials, confirms that the pristine cotton retains its organic, non-carbonized nature. When the cotton is carbonized, these cellulose peaks disappear and are replaced by D band (~1340 cm^{-1}, disordered (sp^3) carbon), and G band (~1580 cm^{-1}, graphitic (sp^2) carbon), indicating transformation from organic cellulose to carbonaceous structure, as shown in Fig. 4c (blue).[17,20] The calculated intensity ratio ($I_D < I_G$) of about 0.9 suggests the presence of a moderately disordered graphitic structure, which is favorable for enhancing ion diffusion and providing additional electrochemical active sites. The Raman spectrum of the 3D-CC@Si sample exhibits distinct Si-related peaks along with the typical peaks of carbon, confirming the successful incorporation of Si into the carbon framework.

To further confirm structural characterization, X-ray diffraction (XRD) analysis is conducted. Fig. 5b shows XRD patterns of SiNPs (black), pristine-cotton (red), 3D-CC (blue), and the 3D-CC@Si composite (dark green). The diffraction peaks of the 3D-CC@Si composite located at ~28.4°, ~47.3°, ~56.3°, and ~69.1° coincide with those of s-SiNPs (black curve and JCPDS No. 27-1402), which indicates the existence of the Si crystal in the composite. Simultaneously, the 3D-CC@Si composite with a broaden peak appeared at ~23.6° is ascribed to the carbonized cotton (blue curve).[21]

To evaluate the electrochemical performance, the cyclic voltammetry (CV) curves of materials were performed at scanning rates of 0.1 mV s^{-1} within a voltage range of 0.01–3.0 V. In the CV curves of the pure Si (Fig. 6a), the broad peak at 0.6–0.7 V is attributed to the side reaction related to the formation of a solid electrolyte interphase (SEI) layer[22,23] which disappeared in the subsequent discharge process. The reduction peaks at 0.17 V can be assigned to the conversion of crystalline Si to amorphous (Li_xSi) phases during the lithiation of silicon and the formation of amorphous Li_xSi phases, which is consistent with the voltage plateau observed in the discharge curve.[24] The anodic scan shows a broad peak around 0.35–0.52 V, is attributed to the dealloying process of Li_xSi, corresponding well to the charge plateau in the galvanostatic charge–discharge profiles.[25] In Fig. 6b, the 3D-CC anode matches to the typical characteristics of amorphous carbon materials. During the first cathodic scan, apparent peak at ~0.35 V was observed, which can be attributed to the formation of a solid electrolyte interphase (SEI) layer and the initial lithiation of amorphous carbon sites.[26,27] The peak observed at ~1.5 V might be due to interactions between lithium ions and the functional groups on the carbonized cotton fiber, as shown in previous reports.[26,28] In the subsequent cycles, CV profiles become more stable and overlap well, indicating the good reversibility of the lithium insertion/extraction processes. Moreover, the relatively high current density observed in the CV curves indicates strong electrochemical activity and efficient charge-transfer kinetics within the composite anode. This behavior suggests that the 3D-CC anode provides excellent electrical conductivity and abundant active sites for Li^+ storage, facilitating rapid lithiation/delithiation processes. As shown in Fig. 6c, the CV curves of the 3D-CC@Si anode with 20 wt% Si display distinct cathodic peaks associated with both the Si component and the 3D carbon framework during the initial cycle, indicating the simultaneous contribution of lithium alloying with Si and lithium storage within the carbon matrix. In subsequent cycles, the CV profiles become more stable and exhibit better overlap compared with those of the pure Si electrode, suggesting improved reversibility of the lithiation/delithiation processes. This behavior can be attributed to the synergistic effect between Si nanoparticles and the conductive three-dimensional carbon scaffold, which enhances electronic conductivity, facilitates Li^+ transport, and effectively mitigates the volume expansion of Si during cycling.[25]

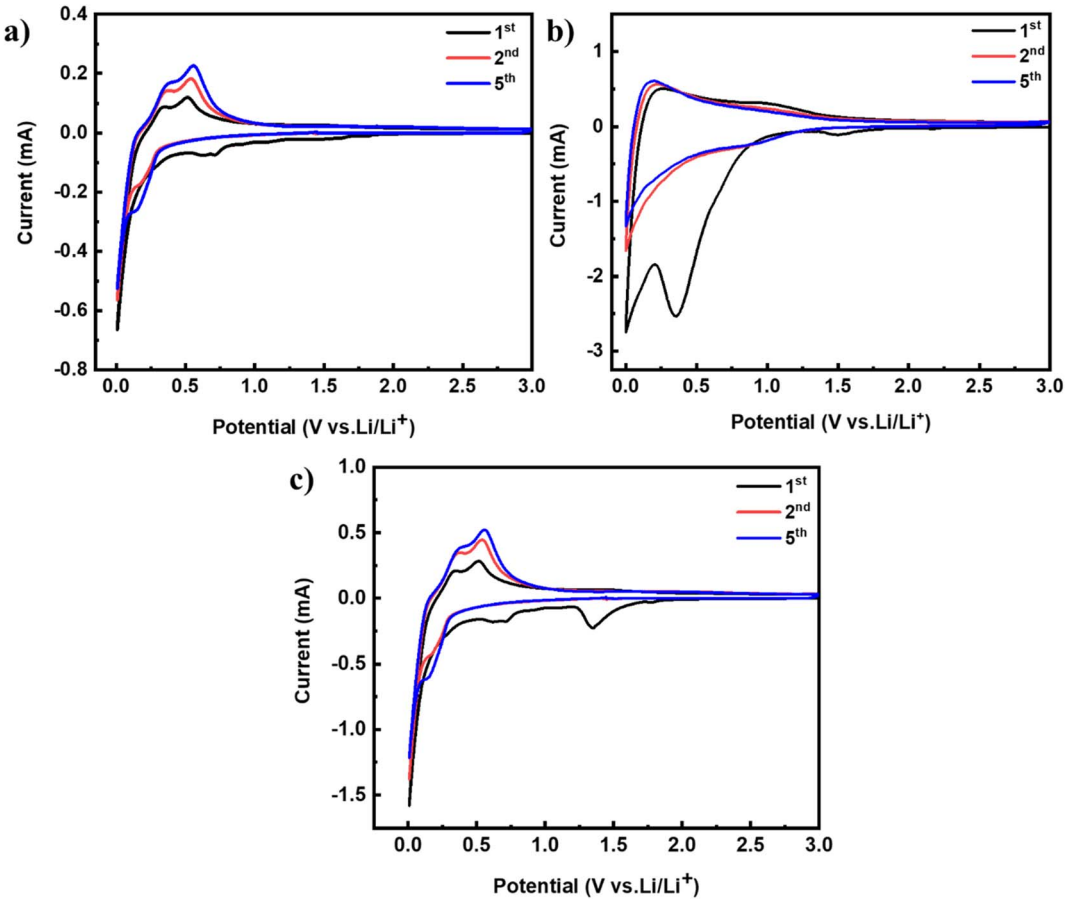

Fig. 6 CV curves for pure Si (a) 3D-CC (b) and 3D-CC@Si (c) electrode at a scanning rate of 0.1 mV s^{-1} within a voltage range of 0.01–3.0 V.

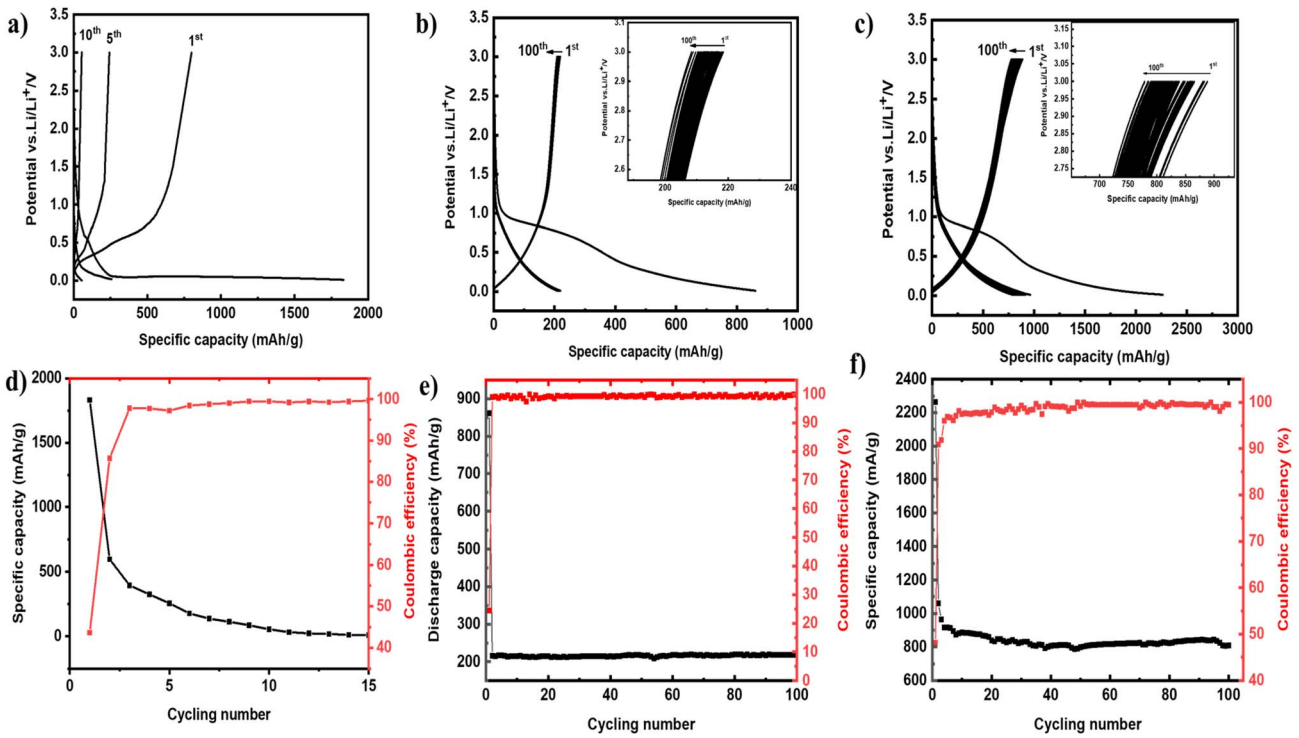

Fig. 7 Charge–discharge profiles and cycling performance of (a and d) pure SiNPs, (b and e) 3D-CC and (c and f) 3D-CC@Si (20wt% Si) electrodes.

The charge–discharge curves of the samples were investigated in coin-type half cells. Fig. 7a displays the typical charge–discharge profiles of the Si anode at different cycles within a voltage window of 0.01–3 V. The electrode delivers an initial discharge capacity of ~1800 mAh g^{-1} and a corresponding charge capacity of ~799 mAh g^{-1}. However, the capacity decreases rapidly upon cycling, which is consistent with previously reported behavior for Si-based anodes.[29]

For the 3D-CC sample (Fig. 7b), the electrode delivers an initial charge/discharge capacity of ~220 mAh g^{-1} and 862 mAh g^{-1} at a current density of 0.25 C. The initial Coulombic efficiency (ICE) was also estimated ~24.6% (Fig. 7e). The relatively low ICE may be attributed to the following reasons. Firstly, a 3D-CC sample with large surface areas, reactive functional groups and more defects can offer a variety sites for insertion of lithium ions.[26] Secondly, the large initial discharge capacity and irreversible capacity of the 3D-CC electrode mainly originate from lithium consumption during SEI formation and electrolyte decomposition in the first discharge cycle, as reported in previous research.[30] Thirdly, some lithium ions inserted into the deeply inner sites of the carbon structure become irreversibly trapped and cannot be extracted during subsequent delithiation,[26] leading to a reduced first-charge capacity. From 2nd cycle, however, the coulombic efficiency rapidly stabilizes to ~99% (red curve in Fig. 7e), indicating highly reversible lithium insertion and extraction reactions. These results demonstrate

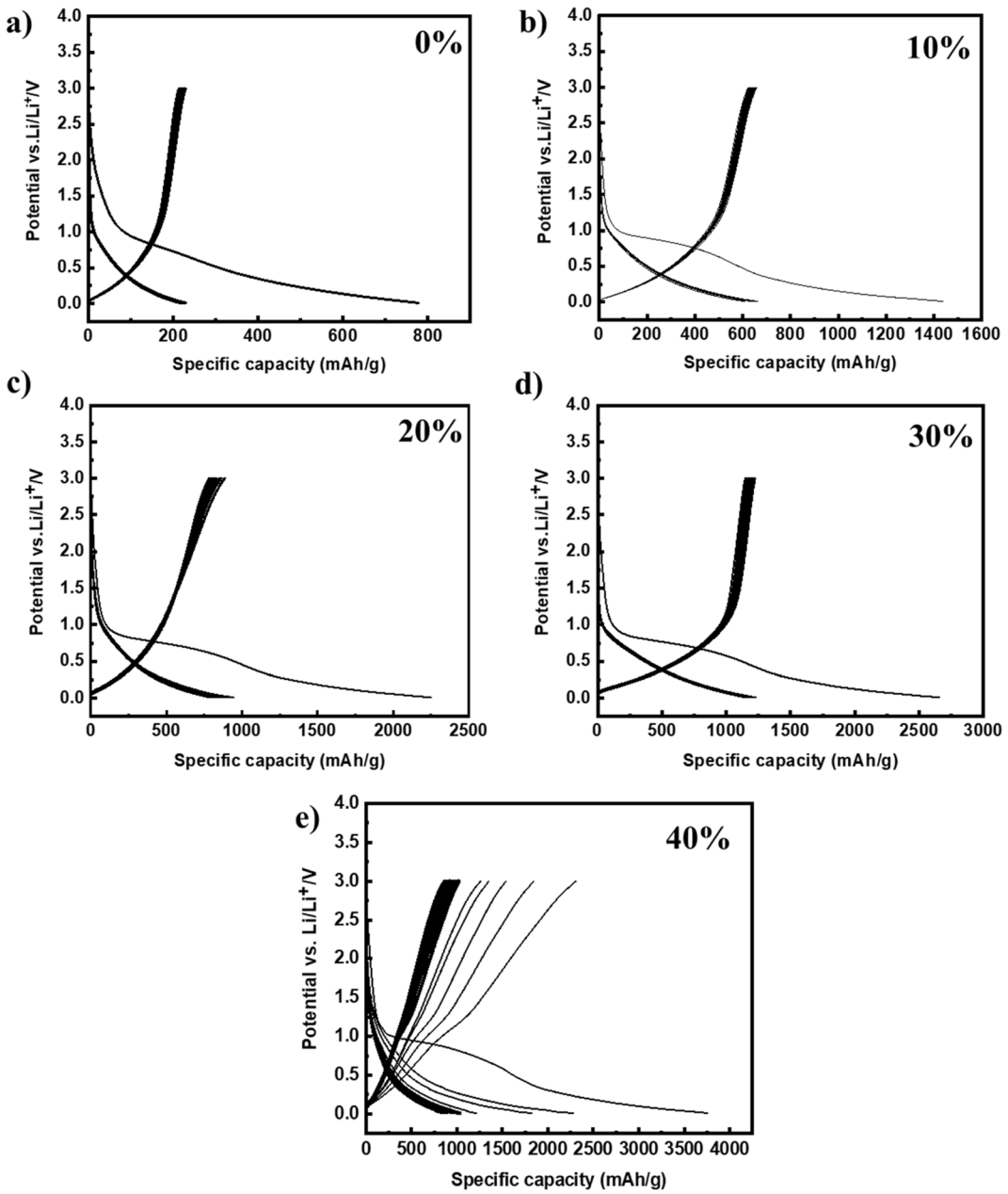

Fig. 8 Effect of SiNP loading on the electrochemical performance of 3D-CC@Si anodes: galvanostatic charge–discharge curves at different SiNP contents of (a) 0%, (b) 10%, (c) 20%, (d) 30%, and (e) 40%.

that the 3D interconnected carbon framework derived from natural cotton provides a robust conductive network and efficient ion diffusion channels, ensuring structural integrity during repeated charge–discharge processes.

The 3D-CC@Si (20 wt% Si) electrode (Fig. 7c) exhibits a markedly enhanced reversible capacity in the range of 800–900 mAh g^{-1} under the same testing conditions. This significant improvement can be attributed to the high theoretical lithium-storage capacity of Si and its uniform distribution within the carbon matrix. The stable coulombic efficiency ~99.8% over extended cycling further confirms the good reversibility and stability of the 3D-CC@Si composite (Fig. 7f). The obtained results implied that the carbon framework not only enhances electronic conductivity but also effectively buffers the large volume changes of Si during lithiation/delithiation, preventing particle pulverization and loss of electrical contact. These results clearly highlight the synergistic effect between Si nanoparticles and the cotton-derived carbon framework, which together contribute to both high capacity and long-term electrochemical stability.

The electrochemical properties of 3D-CC@Si composite further examined by assessing rate performances at different rates ranging from 0.25 C to 1 C over 10 cycles (Fig. S2). The 3D-CC@Si electrode demonstrates significantly elevated discharge capacities of 972, 886, 756, and 665 mAh g^{-1} at the identical rate, respectively. The capacity has subsequently restored to 953 mAh g^{-1} as the current density returns to 0.25 C. In addition, the electrode was further tested at higher current densities of 2 C and 3 C for 100 cycles, as shown in Fig. S3 in the SI. The obtained rate performance of the 3D-CC@Si electrode confirm the structural robustness under high-rate operation.

As study on Si/C composite-based anode materials, the mass ratio between silicon and carbon is a critical parameter for balancing specific capacity and cycling stability. In Fig. 8, the influence of silicon (Si) loading on the electrochemical performance of the 3D-CC@Si composite anode was investigated by varying the Si content from 0% to 40%wt with a step of 10%wt. The 3D-CC electrode (0% Si) exhibits a stable but low reversible capacity of ~220 mAh g^{-1}. When a small amount of Si (~10%) is deposited, the capacity markedly increases to about 620 mAh g^{-1}, reflecting the effective contribution of nanosized Si to Li^+ storage while maintaining acceptable structural stability. At higher Si loadings content of 20–30%, the specific capacity still increases proportionally with the Si loading, while the cycling stability remains well maintained. However, when the Si content is further increased to 40%, the specific capacity can exceed to 2000 mAh g^{-1} during the initial cycles, but a noticeable capacity fading is subsequently observed in the following cycles. After 100 cycles, the capacity retention drops from about 83% for the low-loading sample to only ~52% for the highest-loading one. This degradation is primarily attributed to the drastic volume expansion of Si (~300%) during lithiation, which induces particle pulverization, disruption of the conductive network, and unstable formation/decomposition of the solid–electrolyte interphase (SEI) and SiNPs aggregation. Therefore, the medium Si loading content (~30%) yields the most balanced performance, offering both high capacity and good retention. This behavior highlights the buffering role of the three-dimensional carbon framework derived from cotton fibers. The interconnected porous carbon structure accommodates the volumetric expansion of Si, maintains electrical continuity, and facilitates Li^+ transport pathways. Overall, these findings demonstrate that a moderate Si incorporation into a resilient 3D carbon scaffold provides an effective design strategy for developing high-capacity and durable Si-based anodes for next-generation lithium-ion batteries.

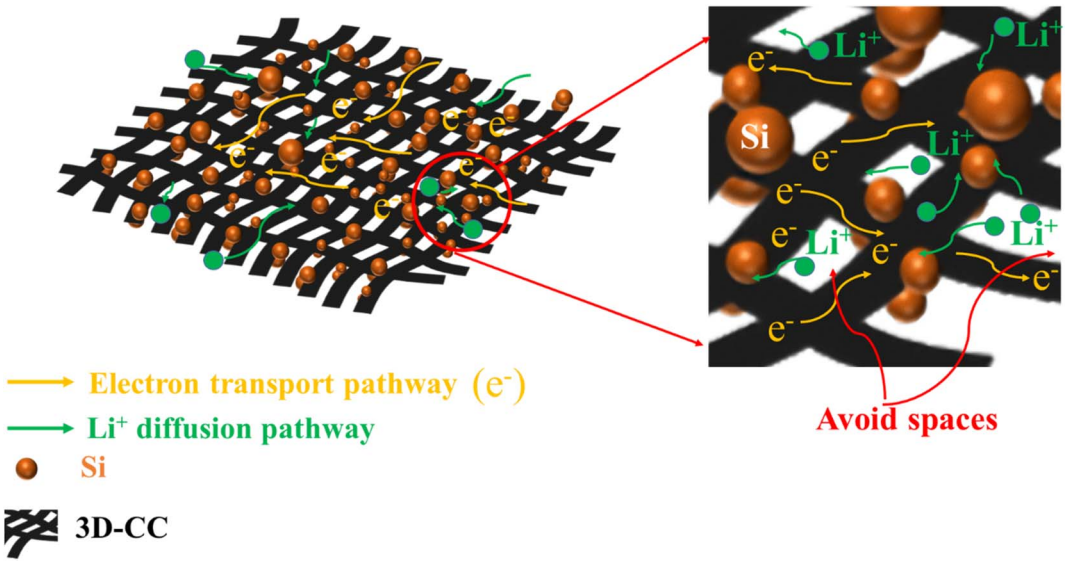

Fig. 9 Schematic illustration of the proposed 3D-CC@Si electrode architecture. SiNPs are uniformly anchored on the interconnected three-dimensional carbon framework derived from cotton fibers. The conductive carbon network provides 3D continuous electron transport pathways and efficient Li^+ diffusion channels, while the porous structure accommodates the volume expansion of Si during lithiation/delithiation processes.

To further clarify the structural design and the underlying mechanisms responsible for the improved electrochemical performance, a schematic illustration of the proposed 3D-CC@Si electrode architecture is presented in Fig. 9. In this structure, SiNPs are uniformly distributed and immobilized on the interconnected 3D-carbon framework derived from carbonized cotton fibers. The conductive carbon network forms a three-dimensional continuous electron transport pathway and facilitates rapid Li^+ diffusion throughout the electrode. Meanwhile, the porous and flexible carbon scaffold not only effectively accommodates the large volume changes of Si during the lithiation/delithiation processes, but also allows the electrolyte to readily penetrate into the internal structure, thereby maintaining structural integrity and stable electrical contact. As a result, this synergistic structural design leads to enhanced electrochemical activity, improved charge-transfer kinetics, and superior cycling stability of the 3D-CC@Si composite electrode.

4. Conclusions

In summary, a sustainable and self-supporting 3D-CC@Si composite anode has been successfully developed using natural cotton as a carbon precursor and silicon nanoparticles as the high-capacity active component. The cotton-derived three-dimensional carbon framework provides a continuous conductive network and mechanical robustness, while uniformly anchored and carbon-coated Si nanoparticles ensure efficient charge transport and stable electrode–electrolyte interfaces. This integrated architecture enables binder-free and current-collector-free electrode fabrication, significantly simplifying the manufacturing process and eliminating the need for environmentally harmful solvents. The synergistic interaction between the 3D carbon scaffold and Si nanoparticles effectively mitigates the volume expansion of Si, suppresses excessive SEI formation, and preserves structural integrity during repeated lithiation/delithiation process. As a result, the 3D-CC@Si anode delivers improved electrochemical performance and cycling stability, highlighting its potential as a scalable and eco-friendly anode design for next-generation high-energy lithium-ion batteries.

Author contributions

Nguyen Van Tu: supervision, conceptualization, methodology, formal analysis, project administration, writing – original draft preparation, validation, writing – reviewing and editing. Pham Van Trinh: formal analysis, investigation. Nguyen Van Chuc: formal analysis, investigation. Cao Thi Thanh: validation, investigation. Bui Hung Thang: formal analysis. Pham Thi Nam: formal analysis, investigation. Nguyen Hoang Tung: formal analysis, investigation. Pham Duy Long: formal analysis, investigation. Nguyen Thanh Tung: formal analysis, investigation. Tran Dai Lam: investigation. Phan Ngoc Minh: formal analysis, investigation. Nguyen Van Hao: formal analysis, validation. Vu Xuan Hoa: formal analysis, investigation. Vu Van Ngoc: formal analysis, investigation. Dinh Trong Thang: formal analysis, investigation. Tran Van Hau: conceptualization, methodology, formal analysis, writing – original draft preparation, validation, writing – reviewing and editing. All authors discussed and approved the paper.

Conflicts of interest

There are no conflicts to declare.

Data availability

The datasets used and/or analyzed during the current study are available from the corresponding author upon reasonable request. In addition, all the data generated or analyzed during this study are included in this article.

Supplementary information (SI) is available. See DOI: https://doi.org/10.1039/d5ra10046a.

Acknowledgements

This work is financially supported by Vietnam Academy of Science and Technology under Project KHCBVL.03/23-24. We also thank the Objective Lab for Agriculture-Bio-Medicine and Energy (VAST/IMS) for the use of facilities.

References

1 J. R. Dahn, T. Zheng, Y. Liu and J. S. Xue, *Science*, 1995, **270**, 590–593.
2 M. Yoshio, H. Wang, K. Fukuda, Y. Hara and Y. Adachi, *J. Electrochem. Soc.*, 2000, **147**, 1245.
3 L. Shi, W. Wang, A. Wang, K. Yuan, Z. Jin and Y. Yang, *J. Mater. Chem. A*, 2015, **3**, 18190–18197.
4 N. Liu, H. Wu, M. T. McDowell, Y. Yao, C. Wang and Y. Cui, *Nano Lett.*, 2012, **12**, 3315–3321.
5 R. Fang, W. Xiao, C. Miao, P. Mei, Y. Zhang, X. Yan and Y. Jiang, *Electrochim. Acta*, 2019, **317**, 575–582.
6 D. Kowalski, J. Mallet, S. Thomas, A. W. Nemaga, J. Michel, C. Guery, M. Molinari and M. Morcrette, *J. Power Sources*, 2017, **361**, 243–248.
7 B.-H. Chen, S.-I. Chuang and J.-G. Duh, *J. Power Sources*, 2016, **331**, 198–207.
8 V. Chabot, K. Feng, H. W. Park, F. M. Hassan, A. R. Elsayed, A. Yu, X. Xiao and Z. Chen, *Electrochim. Acta*, 2014, **130**, 127–134.
9 L. Xu, Z. Quan, F. Wang, A. Lu, Q. Zhao, W. Zhang, Z. Tang, D. Dang, Q. Liu and C. Zhang, *J. Power Sources*, 2025, **656**, 238022.
10 F. Wu, Z. He, M. Wang, Y. Huang and F. Wang, *Nano Res.*, 2022, **15**, 6168–6175.
11 F. Wang, Z. Hu, L. Mao and J. Mao, *J. Power Sources*, 2020, **450**, 227692.
12 W. Wang, J. Du, Z. Xu, Z. Liu, H. Jia, T. Li, Y. Nie and K. Song, *J. Mater. Sci. Mater. Electron.*, 2023, **34**, 809.
13 V.-T. Nguyen, K. Cho, Y. Choi, B. Hwang, Y.-K. Park, H. Nam and D. Lee, *Biochar*, 2024, **6**, 96.
14 X. Zhu, Y. Zeng, X. Zhao, D. Liu, W. Lei and S. Lu, *EcoEnergy*, 2025, e70000.

15 W. He, H. Luo, P. Jing, H. Wang, C. Xu, H. Wu, Q. Wang and Y. Zhang, *J. Alloys Compd.*, 2022, **918**, 165364.
16 Z. Meng, Z. Xu, H. Li, H. Xiong, X. Liu, C. Qin and Z. Wang, *Energies*, 2025, **18**, 972.
17 Q. Pan, J. Zhao, B. Xing, S. Jiang, M. Pang, W. Qu, S. Zhang, Y. Zhang, L. Zhao and W. Liang, *New J. Chem.*, 2019, **43**, 15342–15350.
18 Z. Yi, N. Lin, T. Xu and Y. Qian, *Chem. Eng. J.*, 2018, **347**, 214–222.
19 M. Adebajo, R. Frost, J. Kloprogge and S. Kokot, *Spectrochim. Acta A Mol. Biomol. Spectrosc.*, 2006, **64**, 448–453.
20 H. Yue, S. Chen, S. Zhang, X. Yan, W. Li, T. Li, L. Qiao, P. Li, L. Wu and W. Liu, *J. Alloys Compd.*, 2024, **1004**, 175858.
21 J. Zhang, H. Long and P. Zhang, *Text. Res. J.*, 2022, **92**, 3719–3732.
22 J. J. Wu and W. R. Bennett, *2012 IEEE Energytech*, Cleveland, OH, USA, 2012, pp. 1–5.
23 Y. Zhuo, H. Sun, M. H. Uddin, M. K. Barr, D. Wisser, P. Roßmann, J. D. Esper, S. Tymek, D. Döhler and W. Peukert, *Electrochim. Acta*, 2021, **388**, 138522.
24 W. Wang and P. N. Kumta, *ACS Nano*, 2010, **4**, 2233–2241.
25 X. Ding and Y. Wang, *Electrochim. Acta*, 2020, **329**, 134975.
26 K. Yu, J. Li, H. Qi and C. Liang, *Diam. Relat. Mater.*, 2018, **86**, 139–145.
27 C. Padwal, H. D. Pham, L. T. My Hoang, S. Mundree, A. K. Nanjundan, S. G. Krishnan and D. Dubal, *ChemSusChem*, 2024, **17**, e202301866.
28 K. Tang, R. J. White, X. Mu, M. M. Titirici, P. A. van Aken and J. Maier, *ChemSusChem*, 2012, **5**, 400–403.
29 G. Zhao, L. Zhang, Y. Meng, N. Zhang and K. Sun, *J. Power Sources*, 2013, **240**, 212–218.
30 L. Wang, Z. Schnepp and M. M. Titirici, *J. Mater. Chem. A*, 2013, **1**, 5269–5273.